Research Article

Steffen Matthias*, Markus Kästner and Eduard Reithmeier

Modeling of imaging fiber bundles and adapted signal processing for fringe projection

DOI 10.1515/aot-2016-0050
Received September 7, 2016; accepted October 4, 2016; previously published online November 9, 2016

Abstract: Fringe projection profilometry is an established technique for capturing three-dimensional (3-D)-geometry data with high-point densities in short time. By combining fringe projection with endoscopy techniques, it is possible to perform inline inspection of industrial manufacturing processes. A new fringe projection system is presented, which uses flexible image fiber bundles to achieve versatile positioning of a compact sensor head. When measuring specimens with highly varying reflectivity, such as technical surfaces on tool geometries, measurement errors increase especially due to the crosstalk between individual fibers in the bundle. A detailed analysis of the transmission properties of the utilized fiber bundles is presented. It is shown that aliasing is avoided due to the non-regular grid structure of a bundle. Different techniques are demonstrated to reduce the effect of crosstalk on the phase evaluation. Measurements of highly reflective technical surfaces with different geometrical properties are shown.

Keywords: crosstalk; fringe projection; heterodyne; image fibers; modeling.

1 Introduction

In order to ensure the operation of machinery, inline inspection of functional elements is a critical part of modern industrial processes. To fulfill this task, measuring devices must meet both time and space constraints. Different techniques are applicable to measure both roughness and geometrical properties of industrial parts [1]. While three-dimensional (3-D) measuring microscopes based on confocal, interferometry, or focus variation techniques are capable of capturing surface properties with a vertical resolution of less than 100 nm, the lateral and vertical measurement ranges are limited. Additionally, the mentioned techniques exhibit increased measuring durations for specimens featuring high vertical range. For the measurement of free-form geometries, such as gearings in industrial processes, optical measurement techniques based on triangulation have been established as an alternative to tactile coordinate measuring machines [2]. While these techniques feature larger measuring volumes, they are usually not applicable for measuring roughness parameters due to their limited vertical resolution.

Fringe projection is an optical measuring technique based on triangulation capable of meeting the time requirements with measurement durations in the range of less than 10 s for obtaining high-density areal geometry information of free-form objects. The basic design of a fringe projection system consists of a single camera and a single pattern projector arranged in a triangle with the specimen. In order to obtain a point cloud of the surface geometry, a sequence of predefined patterns is projected onto the surface and captured with the camera. By evaluating the deformation of the patterns in the camera images, the relative 3-D position of surface points can be triangulated using the correspondence information and system parameters, such as the triangulation angle and the focal length of the camera and projector.

Unfortunately, the limited access to functional elements and partially occluded geometries in integrated machinery reduces the applicability of commercially available fringe projection devices. A possible solution to overcome the space limitations is the use of endoscopy techniques, which are widely used for imaging tasks in medical applications. Three different approaches may be considered to transport spatial image information: flexible fiber optical bundles, rigid endoscopes consisting of a lens system, and video endoscopes. Each of these techniques has unique properties regarding image contrast, resolution, and flexibility. Next to the detector part,

***Corresponding author: Steffen Matthias,** Leibniz Universität Hannover, Institute of Measurement and Automatic Control, Nienburger Str. 17, 30167 Hannover, Germany, e-mail: steffen.matthias@imr.uni-hannover.de.
http://orcid.org/0000-0002-6479-9742
Markus Kästner and Eduard Reithmeier: Leibniz Universität Hannover, Institute of Measurement and Automatic Control, Nienburger Str. 17, 30167 Hannover, Germany

e.g. the camera, the patterns of the projector may also be transported using flexible or rigid endoscopes. Alternatively, pattern generation at the tip of the sensor is possible using diffraction gratings or dias. This also leads to fixed patterns and limited signal-to-noise ratio (SNR). Advanced techniques for fast inspection, such as inverse fringe projection or adapted patterns, are not possible using a projector at the tip.

The new measuring device presented in this article uses flexible fiber bundles to transport the image information of both the detector (camera) and emitter (projector) path to achieve versatile positioning while maintaining a compact design of the sensor head. Figure 2 shows a close-up photo of the sensor head next to a specimen; the two fiber bundles can be seen on the left. The sensor head measures approximately 15 mm in width, 15 mm in height, and 8.5 mm in depth, including the optics seen on the right. In addition to the flexible positioning, the sensor head is robust to increased temperatures and electromagnetic fields, which is beneficial for the inspection of industrial forming processes [3].

The quality of optical measurements is dependent on the optical properties of the surface. Fringe projection measurements suffer from surfaces with high reflectance, as a large fraction of the light is either reflected away from the camera or leading to highlights resulting in areas with very high intensity. When using fiber bundles, coupled light also leaks to other cores in the bundle, resulting in global deviations in the measured 3-D point cloud data. While it is common to use spray coatings to make surfaces diffuse reflective, this is not possible for in-line inspection. Therefore, this article gives an overview over the transmission properties of the fiber bundles employed in the fiber-optic fringe projection system. A combination of different techniques is presented to reduce the influence on phase measurements, followed by examples of technical surfaces and corresponding 3-D measurements.

2 Fiber-optic fringe projection

Figure 1 shows a schematic of the fiber-optic fringe projection system. The general setup consists of a base unit, which houses both camera and pattern generation unit, and a sensor head. The sensor head and base unit are coupled using two flexible coherent imaging fibers (FIGH-100-1500N by Fujikura Ltd., Tokyo, Japan) with 100.000 individual cores forming an active area of 1.4 mm in diameter. Each fiber bundle has a total diameter of 1.7 mm, a length of 1000 mm, and a minimum bending radius of 200 mm. For coupling of the generated projection patterns to the projection fiber, a microscope objective with a numerical aperture of 0.2 is used. The patterns are generated with digital micromirror device (DMD) from Texas Instruments Incorporated (Dallas, TX, USA), allowing for the generation of arbitrary projection patterns with a resolution of 1024 by 768 pixels. Grayscale pattern sequences with a resolution of 8 bit can be displayed with a maximum pattern rate of 290 Hz. For illumination, either a LED is employed as an incoherent light source with reduced coupling efficiency, or a laser light source, which introduces speckle artifacts when projecting the patterns on rough surfaces. The experiments in this work are performed using the LED setup for illuminating the patterns. The camera is a Point Grey Research Inc. (Richmond, British Columbia, Canada) GS3-U3-23S6M-C industrial camera featuring a CMOS sensor with resolution of 2.3 megapixels. As discussed later in Section 3.1, the resolution is sufficient to avoid aliasing artifacts when imaging the fiber's grid structure. The sensor is capable of capturing images at rates up to 162 Hz. According to the datasheet, the sensor features a dynamic range of 66.29 dB. The system is capable of capturing images with higher dynamic range by taking exposure series of fringe patterns on a specimen. Measuring times are below 2 s for diffuse reflective objects. The far ends of both fiber bundles are fixed at the compact sensor head, which features gradient-index (GRIN) optics by GRINTECH Gmbh (Jena, Thuringia, Germany) with a

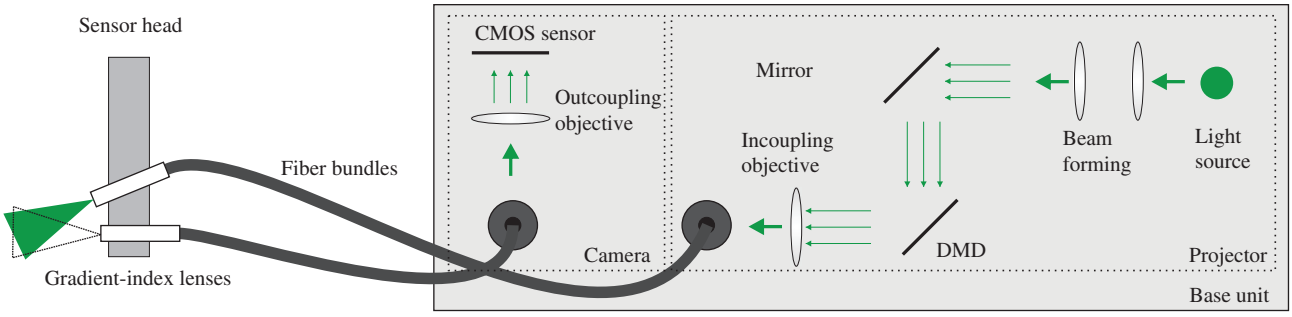

Figure 1: Schematic of the fiber-optic fringe projection system.

diameter of 2 mm and a working distance of 10 mm, resulting in a measuring volume of about 5 mm × 5 mm × 2.5 mm. Optional mirror prisms, such as seen in Figure 2, may be used to rotate the angle of projection and imaging by 90°. For larger measuring volumes, GRIN optics with a working distance of 20 mm is available.

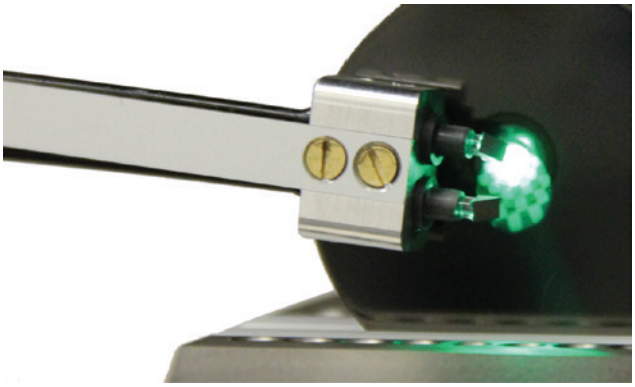

Figure 2: Sensor head of the fiber-optic fringe projection system.

3 Image formation model for optical fiber bundles

Apart from the number of cores, different types of optical fibers are available. Incoherent optical fiber bundles do not have ordered end faces and require a calibration step to recover the ordered image [4]. In comparison, coherent image fibers have ordered end faces and allow for direct view of the remote images. The following analyses and experiments are valid for coherent fiber bundles.

This section describes several properties of coherent fiber bundles and presents a model of the image transport via the fibers. Characteristic parameters are estimated for the fiber bundles used in the fringe projection system described in Section 2. In order to estimate the model parameters, a single fiber bundle has been used to directly connect the projection unit and the camera. This allows for the generation of well-defined input patterns to the fiber bundle while observing the output with the camera.

Figure 3 shows the model used to describe the image transport in the optical fiber bundle. Followed by a 2-D sampling of the image at the far end of the fiber, the sampled image is convolved with a model for crosstalk. Less significant influences are considered as noise with different spectral characteristics.

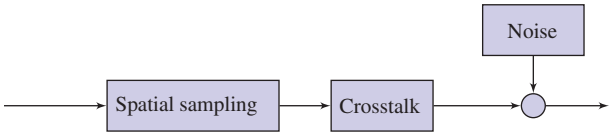

Figure 3: Schematic of imaging model for fiber bundles.

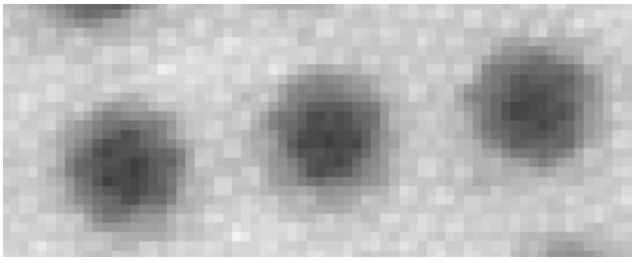

Figure 4: Grid structure in camera image.

3.1 Sampling

Owing to the discrete number of pixels of the fiber bundles, image information at the surface is sampled, with the sampling grid being dependent on the fiber structure of the imaging fibers. Common grid structures are hexagonal grids or randomly oriented fibers [5]. The type of fiber used for the fiber-optic fringe projection system features a randomly distributed fiber pattern. A close-up view of the grid structure can be seen in Figure 4. The individual fiber cores vary slightly in size as well as the grid orientation. Compared to sampling on a regular grid, for example, a camera sensor, the stochastic distribution of sampling points has the advantage of avoiding aliasing when sampling images with higher frequencies than half the sampling frequencies [6]. Despite the relatively low resolution of the fibers, no discrete aliasing artifacts are visible in the transported images. A theoretical analysis for both hexagonal and random grid structures is shown in Ref. [7], which also gives an estimation of the transmission properties.

Figure 5 shows the Fourier magnitude spectrum of a 1-D fringe pattern transmitted via the fiber bundle. The fiber grid structure is visible as the outer ring; the average period of the grid is estimated to 2.88 pixels and is plotted as the dashed red circle. The fringe pattern is visible in the form of two peaks, which are significantly above the Nyquist frequency of an ordered sampling pattern of similar frequency. Wider noise spreads in all directions as a result from the stochastic sampling of the high-frequency patterns. However, no discrete aliasing of the pattern occurs.

3.2 Crosstalk

Owing to the proximity of the individual cores, a certain amount of light transported in an individual fiber is

coupled to the neighboring fibers. Crosstalk can reduce the transmission capabilities of high-resolution image fibers significantly, so that a comparison of the number of cores is not necessarily a valid comparison for the resolution of fiber bundles [8]. A theoretical analysis of inter-fiber coupling in fiber bundles depending on the shape of the fiber cores is given in Ref. [9]. Core separation is limited by the core-to-core distance and the index difference between the core material and the common cladding.

The following evaluations aim to estimate the transfer function and average point spread function for the transported image by modulating the input. In Ref. [10], the PSF of individual fiber cores in a fiber bundle is measured. The evaluations in this section aim to estimate not the PSF of individual cores but the transfer function image transmission via the full active area of the fiber using incoherent illumination. The result of the analysis is a global average of the local transfer functions.

Projecting point patterns with the pattern generator to illuminate individual fibers to directly sample the point spread is not feasible as accurate phase matching between the point pattern and the fiber would be required due to the shift invariance of the sampling process [11]. Thus, a 1-D squared cosine sweep is used to measure the averaged transfer function. The fringe patterns are generated in 1-D according to Eqs. (1) and (2).

$$I_{pos}(u, v) = 0.5 + 0.5 \cdot cos(2\pi f \cdot u) \tag{1}$$

$$I_{neg}(u, v) = 0.5 - 0.5 \cdot cos(2\pi f \cdot u) \tag{2}$$

By projecting an inverted pattern and subsequent subtraction, the DC component of the fringe patterns can be suppressed. In order to reduce the influence of the outer fiber boundaries, all images are multiplied with a Hamming window. The attenuation at each frequency is obtained by calculating the discrete Fourier transform (DFT) and locating the bin with maximum amplitude. The attenuation is calculated relative to the value of the DC component of the patterns, which is constant for all frequencies. Owing to the observation in camera pixels, all frequencies are given relatively to the sample rate of the camera.

Figure 6 shows the magnitude response measured for frequency sweeps in both the vertical and horizontal dimension of the projector matrix. The transfer function is approximately logarithmic in the measured band, as can be seen from the logarithmic fit. Both orientations of the input patterns exhibit similar attenuation in the measured range, confirming the invariance of the fiber grid to rotation. Also visible is an offset of the low-frequency components with ω approaching zero. The fit shows a relative attenuation of the DC component of the DFT of

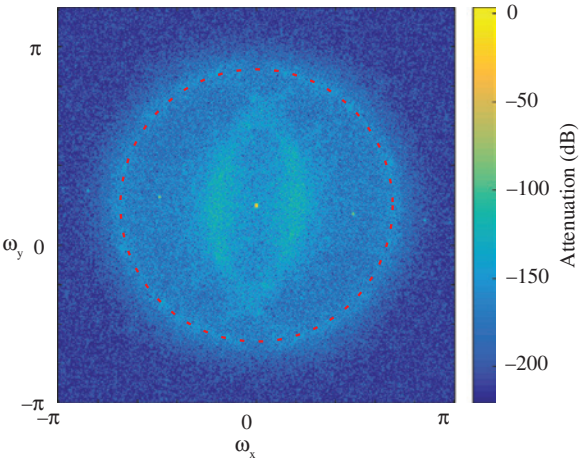

Figure 5: Magnitude spectrum of 1-D fringe pattern captured through fiber bundle.

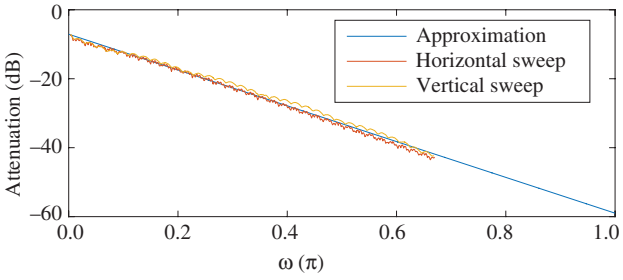

Figure 6: Measured and fitted 1-D magnitude response.

$k = 5.95$ dB $= 1.9854$ compared to the logarithmic fit of the higher frequencies. Unfortunately, due to the resolution of the DFT for low frequencies, accurate estimation of the low-frequency fractions is not possible, leading to an inaccurate model for these components. Figure 7 shows the result from a 1-D step function. The low-frequency components of the PSF can clearly be seen slowly decreasing with growing distance to the step.

The 1-D estimate for the PSF is obtained by assuming zero phase (the PSF is centered at 0) and calculating the

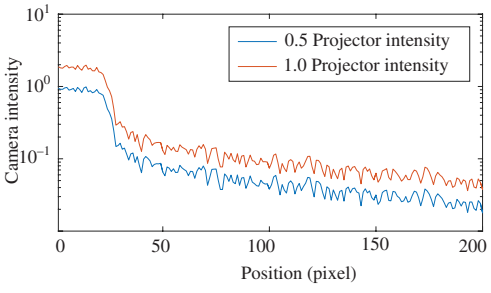

Figure 7: Measured 1-D step response.

inverse DFT of the fitted transfer function. Assuming circular symmetry, the 2-D PSF can be calculated using the McClellan transform [12]. Figure 8 shows the cropped estimated 2-D PSF.

3.3 Noise

Effects not completely modeled by the transfer function are considered as noise. The influence of the individual effects on phase measurements will be discussed in Section 4. Different factors contribute to the transported image:

- **Aliasing** While the fiber bundles do not suffer from discrete aliasing artifacts, wider-band noise appears when transporting high-frequency signals, as shown in Section 3.1. The effect is reduced when using the GRIN optics for coupling in the sensor head, as higher frequencies are attenuated due to the limited resolution of these optics.
- **Variable attenuation of pixels** Another aspect is the individual attenuation of the fiber cores. Owing to different fiber coupling as well as varying attenuation of the individual fibers, a constant wideband modulation is applied to the images. An evaluation of spatial noise on 2-D and 3-D captured with the endoscopic system is presented in Ref. [13] for diffuse reflective targets.
- **Global grid structure** Figure 5 shows the Fourier transform of the fully illuminated fiber. The grid structure is clearly visible in the form of a ring overlaid in the spectrum.
- **Local grid structure** Owing to the local directionality of the grid structure, the estimated PSF in the previous section deviates on a local scale. This leads to inaccuracies when trying to model small-scale crosstalk effects.

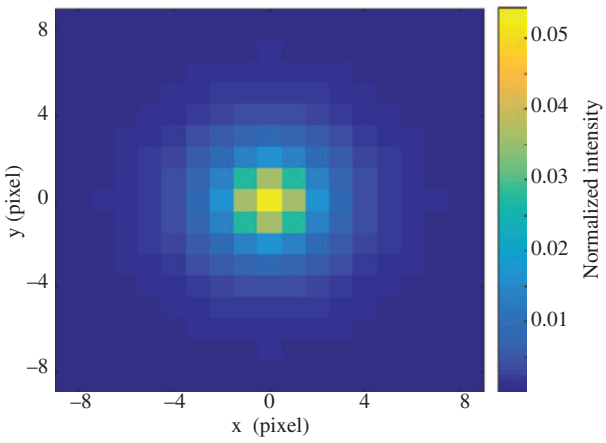

Figure 8: Estimated crosstalk model.

4 Compensation for fringe projection

To obtain a 3-D measurement of the specimen's geometry by fringe projection, points are triangulated using corresponding points on the camera and projector matrix and a model of the measuring system. Thus, an essential step in performing measurements is to determine the camera-projector correspondences. Common patterns for this task are either 1-D squared cosine patterns or Gray-coded binary patterns [14]. The spatial phase of the patterns captured on the camera side encodes both the position of the emitting line on the projector matrix and the geometry of the specimen. By calculating the encoded phase, the process is robust to modulations in amplitude, which occur on objects with varying reflectivity. The pattern sequences are, however, not invariant to convolution, which occurs, for example, in the fiber model as described in Section 3. Based on a description of the mathematical formulation of camera intensity fringe patterns, the effects from the fiber's properties discussed in Section 3 on phase evaluation are discussed. Binary patterns suffer from similar effects due to the need of an adaptive threshold.

The images in a fixed-frequency phase-shift sequence can be described by Eq. (3), where (u, v) defines the position of a pixel in the camera matrix.

$$I_n(u, v) = (B(u, v) + A(u, v) \cdot cos(\phi_n(u, v))) * psf(u, v) + \epsilon \tag{3}$$

where A describes the spatial amplitude modulation, for example, from differences in surface reflectivity, and ϕ is the local phase angle. B consists of both the constant component of the patterns and light from external sources. Parameter ϵ is added noise in the imaging process, while *psf* is the model for the optical system.

The index $n = 1, \ldots, N$ denotes the position of the image in the equally shifted sequence. According to Eq. (4), the local phase values of a pattern in the sequence are shifted equally over a single period.

$$\phi_n(u, v) = \phi(u, v) + n\frac{2\pi}{N} \tag{4}$$

In case *psf* is the δ function (ideal transmission) and $\epsilon = 0$, the phase of the pattern can be obtained by rotating the patterns on a common complex plane and calculating the argument of the accumulated vectors:

$$I_{real}(u, v) = \sum_{n=1}^{N} I_n(u, v) cos\left(n\frac{2\pi}{N}\right) \tag{5}$$

$$I_{imag}(u, v) = i \cdot \sum_{n=1}^{N} I_n(u, v) sin\left(n\frac{2\pi}{N}\right) \quad (6)$$

$$\phi(u, v) = arg(I_{real}(u, v) + I_{imag}(u, v)) \quad (7)$$

Owing to the rotation, parameter B in Eq. (3) is multiplied with 0. Thus, any light from external sources is suppressed, as long as it is not varying over the captured phase-shift sequence. Also, by calculating the phase in Eq. (7), amplitude modulations by A have no further influence. Apart from the local reflectance of the specimen, this temporally constant amplitude modulation is also capable of modeling the varying attenuation of the individual fibers as well as the fiber's grid structure (see Section 3.3).

In case *psf* is not the δ function, as described in Section 3.2, the suppression of external light sources is still valid, as long as B and the PSF are constant over time. However, due to the convolution of the phase-shift pattern images according to Eq. (3), each pattern is independently distorted. Considering the Fourier transformation of Eq. (3), the pattern spectrum is convolved with the Fourier transform of the reflectance of the surface. This effectively leads to an increased bandwidth requirement of the image. For $A(u, v) \neq 1$ (or a non-symmetric PSF), this leads to a distorted estimation of the local phase. These phase errors are increasing with the dynamic range of A. Although deviations in the phase measurement may be reduced to a certain extent by increasing the number of phase-shift images, this will lead to an increased measuring time.

In conclusion, for a non-biased phase evaluation, the optical system must feature a linear magnitude response and zero phase with sufficient bandwidth. The bandwidth requirements are defined by the geometry of the specimen as well as the dynamic range of the reflectance. As the fiber bundles do not feature a linear magnitude response, it must be compensated by digital signal processing.

Figure 9 shows the signal-processing chain to reduce fiber artifacts in the phase measurements. After capturing the pattern sequences, all images are windowed using a 2-D Tukey window with $\alpha = 0.1$ (10% taper) to decrease ringing artifacts at the fiber's edges in the later processing stages. Table 1 gives a short overview of the compensation for a number of the properties of the optical fiber bundles.

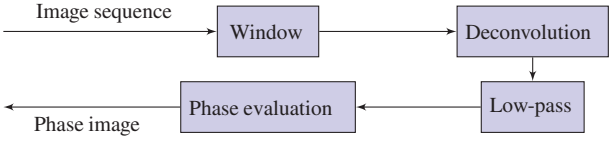

Figure 9: Schematic of imaging model for fiber bundles.

Table 1: Artifacts and compensation.

Artifact	Compensation
Fiber crosstalk	HDR imaging, deconvolution
Fiber structure, cladding	Low-pass filter
Variable attenuation of fibers	Phase evaluation
Low-frequency crosstalk	Heterodyne phase unwrapping

4.1 Deconvolution

The convolution with the PSF, as described in Eq. (3), can be compensated by the convolution of the image with the inverse PSF. However, due to the decreasing SNR for higher frequencies, this will also lead to an amplification of noise. Thus, direct inversion of the transfer function estimated in Section 3.2 is not feasible. Deconvolution algorithms introduce a regularization term or work iteratively in order to avoid the amplification of noise to improve the estimate of the restored image.

For the results presented in Section 5, the Richardson-Lucy iterative deconvolution algorithm [15] is used. As a trade-off between restoration and processing time and noise amplification, the number of iterations has been empirically chosen to 2 based on evaluations on specimens similar to the objects described in Section 5. A higher number of iterations lead to no significant further reduction in the measured deviations from the reference geometries. An additional factor taken into account is the reduction in processing times for lower iteration counts, which benefits the fast inspection of geometries. In Ref. [16], certain convergence properties of the Richardson-Lucy algorithm are studied. It is shown that the restoration of lower frequency components, which dominate the camera images captured via the fiber, converge faster than higher frequencies. Higher frequencies suffer from a lower SNR ratio, due to the transmission properties of both the GRIN optics used in the sensor head and the imaging fibers. Therefore, the improvement in restoration quality by increasing the number of iterations is limited.

Owing to the properties of the deconvolution algorithms and the limitations of the fiber model, low-frequency components of less than a single fringe period cannot be compensated for properly.

4.2 Filter design

As described in Section 3, the bandwidth of the fibers is not limited by the average sampling frequency according to the Nyquist theorem because of their stochastic

sampling behavior. Nevertheless, the SNR is decreasing for higher frequencies due to the attenuation of the signal by the transmission properties of fiber and optics. Additionally, the grid structure of the fibers is overlaid in the spectrum. Therefore, a low-pass filter is applied to attenuate high-frequency noise prior to the phase evaluation.

Research has been published on the removal of the so-called pixelation artifacts in imaging fibers. In Ref. [5], a low-pass filter is applied at half the average sampling frequency of the fibers with a sharp roll-off. In Ref. [17], 2-D Gaussian filters with different standard deviations are evaluated. Alternatively, subpixel localization of fiber core centers and interpolation has been suggested in Ref. [18].

As discussed in the introduction of this section, the digital filter applied to the captured images must feature a linear magnitude response in the pass band to avoid errors in the phase evaluation stage. Gaussian filters are, thus, not suitable for phase imaging as a result of their attenuation in the pass band. As described in Ref. [18], subpixel localization of fiber centers and interpolation offer no benefit over simple low-pass filtering for 2-D imaging. Owing to the computational complexity and resolution requirements for the camera, it is not suitable for the high pattern rates required for in-line inspection.

Therefore, a low-pass filter has been selected as a prefilter for the phase evaluation stage. Based on empirical evaluations of measurements on different objects, the pass band edge has been defined in normalized frequency at $\omega_{pass} = 0.4$ and the stop edge at $\omega_{stop} = 0.6$. A slow roll-off is selected to avoid ringing in the time domain. The attenuation in the stop band has been set to $A_{stop} = -40$ dB and the pass band ripple to $A_{pass} = 0.5$ dB. The filter has been designed as a 1-D FIR filter using the equiripple method and transformed to a 2-D FIR filter using the McClellan transform.

4.3 Phase unwrapping

For fringe patterns with more than one period, the phase evaluation in Eq. (7) will lead to an ambiguous phase image due to the range of the local phase being limited to $-\pi \ldots \pi$. To be able to use fringe patterns with higher frequencies, which are more robust to noise, a phase-unwrapping step is required to solve this ambiguity. Temporal phase unwrapping using a sequence of increasing frequencies is commonly selected for this task [19]. Alternatively, the unwrapping may be performed using, for example, Gray-encoded binary patterns.

Owing to the strong low-frequency components in the point-spread function of the optical fiber bundles, especially image captures of projected patterns with a single fringe period suffer from crosstalk. As the higher frequency phase maps are unwrapped using the single-period patterns, for situations with significant crosstalk, the unwrapping will fail. As unwrapping errors are effectively steps of multiples of 2π, large deviations in the triangulated data will follow. Gray-encoded patterns suffer from the same problem, as the most significant bit is also encoded in a pattern with a single period.

To overcome these problems, a heterodyne unwrapping method is used for unwrapping the higher-frequency phase images [20]. This results in only high-frequency patterns being projected, which feature a higher SNR. The single-period phase map is then acquired by virtually mixing the higher frequencies and calculating the phase of their beat frequency.

5 Results

Figure 10 shows a photo of the two objects used for evaluation. The first object is a polished tactile ball probe with a diameter of 2 mm. In order to reduce specular reflections on the polished surface, the object has been treated by plasma ion nitriding, which is a common treatment of industrial tool steels for hardening. The second specimen is a hard coated planar surface with a circular defective spot in the coating. A CrAlCN coating is used in this case, which has been applied to the substrate material by employing a magnetron-sputtering process. In the context of sheet-bulk metal-forming processes, the coating is used to modify the tribo-mechanical properties of the tool surface [21] and features a roughness average R_a of less than 500 nm. Reflectance of the coated surface areas is dominated by specular reflection, while the defective or

Figure 10: Photograph of the specimens.

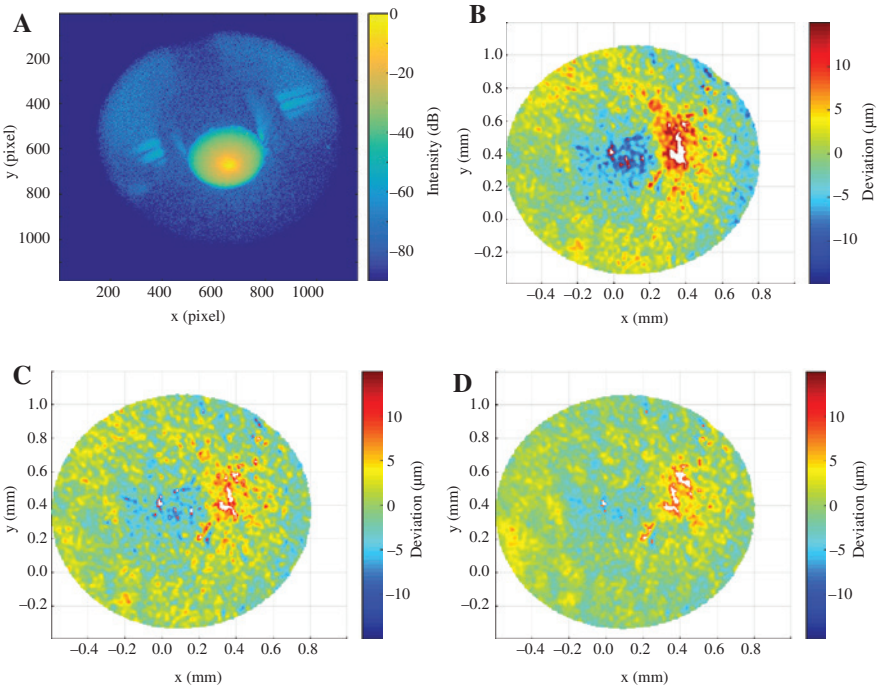

Figure 11: Measurements on spherical object. (A) Magnitude image. (B) Deviations without deconvolution. (C) Deviations with fiber model deconvolution. (D) Deviations with fiber and GRIN model deconvolution.

non-coated spot on the specimen is dominated by diffuse reflection.

The spherical object is shown to demonstrate the influence of high-frequency crosstalk, while the planar object introduces low-frequency crosstalk effects in the measurements. All measurements have been performed using four phase-shift patterns at three different frequencies for unwrapping. The exposure times for capturing the HDR pattern images have been adjusted to capture the specimens without overexposed spots. In addition to the PSF measured for the fiber in Section 3.2, a second PSF has been measured for image transport via the fiber and in-focus coupling using a GRIN lens from the sensor head. Both due to the differences in coupling and the PSF of the lens, the combined PSF is a more complete model of the detector path. A comparison of both models allows to qualitatively compare the influence of the optics and the fibers on the measurements.

5.1 Spherical surface

Figure 11A shows the fringe amplitude of a phase measurement of the spherical object. Owing to the surface angles, a large intensity gradient is visible especially in the neighborhood of the highlight.

In order to analyze the local effects on the 3-D data, a best-fit sphere has been fitted to all measurements. One percent of the data points with the largest deviations to the fitted reference has been discarded to remove outliers. Figure 11B shows the deviations for a measurement without applying the deconvolution signal-processing stage. Next to the highlight, strong deviations are evident due to interference from crosstalk effects. Figure 11B and C show the deviations for deconvolution using either the fiber model or the combined model for fiber and GRIN coupling lens. Both methods reduce the influence of the highlight significantly, although slight deviations in the direct proximity to the highlight remain. For a quantitative analysis, the standard deviations of the measured point to sphere distances are shown in Table 2. By applying devonvolution of the fiber and GRIN model, the standard deviation can be reduced by more than 35%.

Table 2: Standard deviations for spherical object.

No modeling	Fiber model	Fiber and GRIN model
3.3 µm	2.6 µm	2.1 µm

5.2 Coated planar surface

Figure 12A shows an image of the fringe amplitudes on a CrAlCN-coated planar surface. A defect spot in the coating

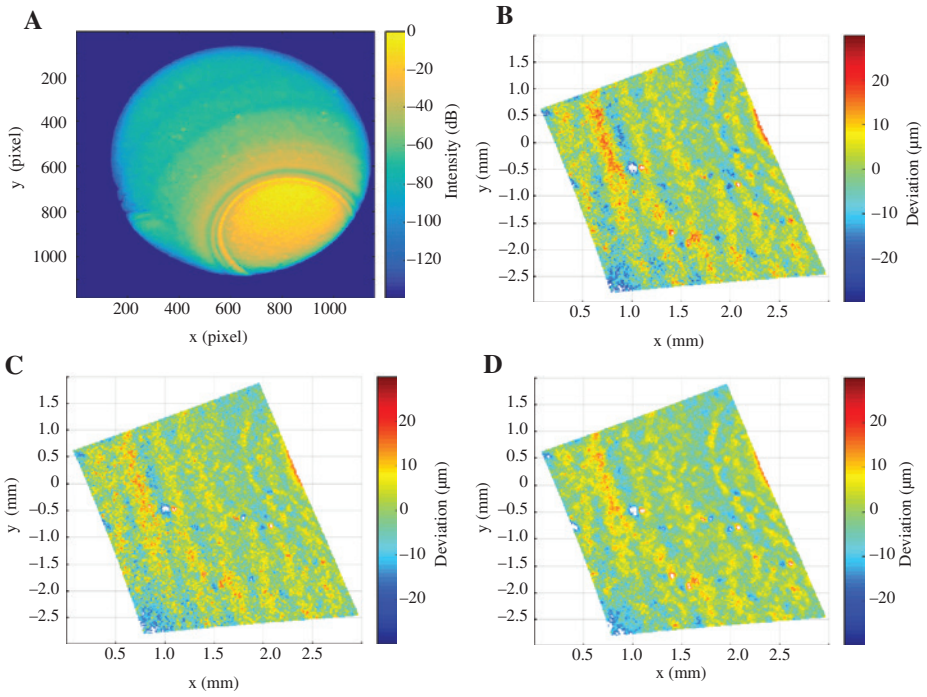

Figure 12: Measurements on planar object. (A) Magnitude image. (B) Deviations without deconvolution. (C) Deviations with fiber model deconvolution. (D) Deviations with fiber and GRIN model deconvolution.

can be seen on the right. Owing to the high specular reflectance of the coated areas, the light is reflected away from the camera, leading to an attenuation of −60 dB to −80 dB for these areas relative to the intensity measured at the defect spot. This introduces low-frequency crosstalk components, similar to the step measurement shown in Section 3.2, to the images. When employing the common temporal phase-unwrapping technique featuring single period patterns, phase unwrapping in the areas with highly attenuated intensity will completely fail, leading to unusable measurements. The results in this section are obtained using the heterodyne phase-unwrapping method as explained in Section 4.3.

Similar to the evaluation for the spherical object, a plane has been fitted to the measured data points. To filter outliers, the 1% of the points with the largest distance to the best-fit plane has been discarded. Figure 12A shows the deviations to the best-fit plane without applying deconvolution to the pattern images. Periodic deviations in the orientation of the projected fringes are visible due to the low-frequency crosstalk. In direct comparison, the deviations are reduced in Figure 12B and C after applying the deconvolution stage. However, the periodic structure is still evident.

As discussed in Section 4.1, the low-frequency components of the fiber PSF cannot be compensated due to limitations in measuring the attenuation at low frequencies and in the deconvolution algorithms. The reduction of the periodic structures is a result of compensating the relative attenuation of the higher frequencies.

Table 3: Standard deviations for planar object.

No modeling	Fiber model	Fiber and GRIN model
6.0 µm	5.4 µm	4.9 µm

Table 3 lists the standard deviation of point-plane distances to quantify the deviations. Despite remaining influences of the low-frequency crosstalk, the standard deviation of point-plane distances is reduced by 1 µm after applying the deconvolution.

6 Discussion

Especially, the heterodyne phase-unwrapping method is beneficial for measuring objects with varying reflectivity, as seen in Section 5.2. By projecting only high-frequency patterns, the unwrapping algorithm is robust to low-frequency crosstalk, enabling the measurement of areas with low intensity relative to the complete image. However, due to limitations in the model and deconvolution algorithms, frequency components of less than a single period in the PSF cannot be compensated. Thus, slight interference in

the form of periodic deviations remains for situations with significant low-frequency crosstalk. Despite these limitations, the measurements showed the capability of detecting deviations larger than 15 µm in scenes with a dynamic range of up to 80 dB, a difference of 1:10,000 in measured fringe amplitudes.

The measurements of the spherical objects show the influence of higher-frequency crosstalk interference. In the neighborhood of the highlight, deviations in negative direction are present on one side of the highlight and positive direction on the other. A reduction in the standard deviation of point-sphere distances of over 35% could be achieved by applying deconvolution of the fiber and GRIN lens transfer function model.

Artifacts evident in 2-D amplitude images transported by the fiber bundles, such as the varying attenuation of individual fiber cores, and pixelation from the discrete core structure, are much less influential on the demonstrated 3-D measurements as a result from phase evaluation.

To summarize, the remaining deviations can be accounted to the following effects:

- **Low-frequency PSF components** Frequencies close to zero are difficult to compensate using the presented modeling and deconvolution techniques.
- **Local directionality of the fiber structure** While the evaluations in Section 3.2 showed that the estimated PSF is valid for a wide frequency range, on average, on a local level, the fiber grid structure deviates from the model, as each core has a discrete number of neighboring cores in varying arrangement.
- **Bandwidth requirements** Especially, narrow highlights result in larger bandwidth requirements for the detection path due to the convolution of the fringe pattern with the surface reflectance in the frequency domain (see Section 4).
- **Camera and projector nonlinearities** In order to capture the dynamic range of the patterns, the exposure time needs to be varied over a wide range. The larger the range, the larger the effect of nonlinearities in capturing the intensity.
- **Signal-to-Noise** The SNR is especially increased in areas with low intensity and for higher frequency components. Applying deconvolution also increases the noise level, limiting the applicability of the method for certain situations.

Thus, for robust measurements, areas with high-intensity gradients will be masked in the 3-D evaluation, which is similar to the behavior of commercial systems. If further reduction of the measurement uncertainty is required, crosstalk artifacts may be reduced to a certain extent by increasing the number of phase-shift images, at the cost of an increased measurement duration.

7 Summary and outlook

A new fringe projection system is presented, which uses flexible imaging fiber bundles to achieve fast in-line inspection of elements with limited accessibility. Based on experiments, a model for the transmission properties of the fibers has been derived. A combination of different techniques is employed to reduce the effects of inter-fiber crosstalk and enable the measurement of specimens with highly varying surface reflectance. Even in situations with fringe amplitude ratios of 1:10,000 in captured pattern images, the standard deviation of point-reference distances is in the order of 5 µm.

Further modeling of optical components of the system could lead to further improved results. In addition, a specifically adapted deconvolution algorithm could consider the similarities in the image sequence of the phase-shift patterns and, thus, lead to a higher robustness toward noise in the camera images. Furthermore, by modulating the projected patterns adaptively in intensity, the dynamic range in the camera images and, thus, the interference from crosstalk could be reduced.

Acknowledgment: The authors would like to thank the German Research Foundation (DFG) for funding the project B6 “Endoscopic geometry inspection” within the Collaborative Research Center (CRC)/TR 73. Thanks to Dominic Stangier from TU Dortmund for providing the coated specimens used for the measurements in this article.

Funding: Deutsche Forschungsgemeinschaft, (Grant/Award Number: ‘SFB/TR 73’).

References

[1] H. Schwenke, U. Neuschaefer-Rube, T. Pfeifer and H. Kunzmann, CIRP Ann. Manuf. Techn. 51, 685 (2002).
[2] E. Savio, L. de Chiffre and R. Schmitt, CIRP Ann. Manuf. Techn. 56, 810 (2007).
[3] S. Matthias, A. Loderer, S. Koch, M. Gröne, M. Kästner, et al, Prod. Engineer. 10, 51 (2016).
[4] J. Gamo, O. Demuynck, Ó. Esteban, J. L. Lázaro and A. Cubillo, Proc. IADAT (IADAT, Bilbao, Spain, 2005).
[5] C. Winter, S. Rupp, M. Elter, C. Munzenmayer, H. Gerhauser and T. Wittenberg, IEEE Trans. Biomed. Eng. 53, 2035 (2006).
[6] M. A. Z. Dippé and E. H. Wold, ACM Siggraph Computer Graphics 19, 69 (1985).
[7] R. Drougard, J. Opt. Soc. Am. 54, 907 (1964).

[8] X. Chen, K. L. Reichenbach and C. Xu, Opt. Express 16, 21598 (2008).
[9] K. L. Reichenbach and C. Xu, Opt. Express 15, 2151 (2007).
[10] O. Coquoz, Opt. Eng. 34, 2092 (1995).
[11] S. K. Park, R. Schowengerdt and M.-A. Kaczynski, Appl. Opt. 23, 2572 (1984).
[12] J. H. McClellan, in 'Proc. 7th Annu. Princeton Conf. Information Sciences and Systems' (1973) pp. 247–251.
[13] S. Matthias, M. Kästner and E. Reithmeier, in 'SPIE Photonics Europe, SPIE Proceedings', Ed. By F. Berghmans and A. G. Mignani (SPIE, 2016) p. 989905.
[14] S. S. Gorthi and P. Rastogi, Opt. Lasers Eng. 48(IMAC-REVIEW-2009-001), 133–140 (2010).
[15] W. H. Richardson, J. Opt. Soc. Am. 62, 55 (1972).
[16] S. Prasad, J. Opt. Soc. Am. A 19, 1286 (2002).
[17] J.-H. Han, J. Lee and J. U. Kang, Opt. Express 18, 7427 (2010).
[18] S. Rupp, C. Winter and M. Elter, in 'Annual International Conference of the IEEE Engineering in Medicine and Biology Society', (2009) pp. 3677–3680.
[19] J. M. Huntley and H. Saldner, Appl. Opt. 32, 3047 (1993).
[20] H. P. Stahl, in 'San Diego – DL Tentative, SPIE Proceedings', Ed. By C. P. Grover (SPIE, 1990) p. 704.
[21] W. Tillmann, D. Stangier and P. Schröder, Surf. Coat. Technol. (2016). DOI: 10.1016/j.surfcoat.2016.07.110 (in press).

Steffen Matthias
Leibniz Universität Hannover, Institute of Measurement and Automatic Control Nienburger Str. 17, 30167 Hannover Germany
http://orcid.org/0000-0002-6479-9742
steffen.matthias@imr.uni-hannover.de.

Steffen Matthias is a research associate at the Institute of Measurement and Automatic Control at Leibniz Universität Hannover.

Markus Kästner
Leibniz Universität Hannover
Institute of Measurement and Automatic Control Nienburger Str. 17, 30167 Hannover, Germany

Markus Kästner is the head of the department for production metrology at the Institute of Measurement and Automatic Control at Leibniz Universität Hannover.

Eduard Reithmeier
Leibniz Universität Hannover
Institute of Measurement and Automatic Control, Nienburger Str. 17
30167 Hannover, Germany

Eduard Reithmeier is the head of the Institute of Measurement and Automatic Control at Leibniz Universität Hannover.